SOLUTION MINING RESEARCH INSTITUTE

679 Plank Road
Clifton Park, NY 12065, USA
Telephone: 5.1.2.e
www.solutionmining.org

Technical Conference Paper

Microstructural Investigation of Heterogeneous Rock Salt Permeation: Unraveling the influence of Anhydrite and Mega-Grain content on Fluid Transport

5.1.2.e

Microstructure and Pores GmbH, Junkerstraße 93, 52064, Aachen, Germany

5.1.2.e

Nobian Industrial Chemicals B.V., Van Asch van Wijckstraat 53, 3811 LP Amersfoort, The Netherlands

5.1.2.e

IfG - Institut für Gebirgsmechanik GmbH, Friederikenstraße 60, 04279 Leipzig, Germany

SMRI Spring 2024 Technical Conference
22-23 April 2024
Krakow, Poland

Solution Mining Research Institute Spring 2024 Conference

Krakow, Poland, 22-23 April 2024

Microstructural Investigation of Heterogeneous Rock Salt Permeation: Unraveling the influence of Anhydrite and Mega-Grain content on Fluid Transport

5.1.2.e

1Microstructure and Pores GmbH, Junkerstraße 93, 52064, Aachen, Germany, 2Nobian Industrial Chemicals B.V., Van Asch van Wijckstraat 53, 3811 LP Amersfoort, The Netherlands, 3Institut für Gebirgsmechanik GmbH, Friederikenstraße 60, 04279 Leipzig, Germany

Abstract

This study investigates the micro-scale process of permeation behaviour. Permeation is crucial in governing long-term cavern pressure post-abandonment, which is considered crucial for reliable numerical modelling of cavern pressure evolution. Uncertainties persist regarding the most suitable permeation model for upscaling from grain-size to field scales. The investigation focuses on microstructural analyses of laboratory permeation tests conducted on heterogeneous natural rock salt samples. These tests were designed to assess hydraulic properties under varying effective stresses, emphasizing the impact of anhydrite inclusions and mega-grains on fluid flow within the salt matrix. Utilizing a radial flow geometry within a standard triaxial apparatus, experiments were conducted over 30-50 days using saturated brine as the fluid medium while applying a differential stress of 1 MPa. Microstructural analysis integrated micro-CT, optical microscopy, and SEM techniques, providing insights into the intricate pore networks and internal structure of rock salt. Findings highlight preferred permeation pathways such as the interfaces of halite mega-grains with matrix grains and/or with thin anhydrite bands, which can be the dominating pathway compared to also present dilatant matrix-halite grain boundary networks. These results offer valuable insights into permeation behaviour of rock salt, particularly under saturated brine conditions, contributing to a deeper understanding of cavern pressure dynamics and improving future modelling efforts.

Key words: heterogeneous salt, permeation processes, microstructures, laboratory testing, long-term creep behavior, axial (differential) stress, confining pressure, temperature

Introduction

When caverns are abandoned and cavern pressure is no longer controlled via a wellhead, the cavern pressure is increased over time due to thermal effects and continued cavern convergence. The permeation mechanism is thought to act as a relief-mechanism limiting cavern pressure development. The controlling factors are believed to include the microfabric of salt, the state of stress, and the fluid pressure magnitude (Urai et al., 2019). The cavern pressure is limited by an equilibrium state between cavern convergence / cavern volume loss and the outflow of brine through the rock salt. Permeation is therefore one of the dominant factors controlling the long-term cavern pressure after abandonment of caverns (e.g., Brouard et al., 2001, Baumann et al, 2022).

While the effect can be implemented in numerical codes simulating cavern pressure evolution, such models are only reliable if the underlying assumptions on the microphysical processes governing permeation are correct. To date, there is no consensus on what permeation model is best for upscaling permeation behaviour, from operating on grainsize scales to field scales. General approaches based

on laboratory tests suggest a relation between rock salt permeability and the effective stress (i.e., Fokker 1995, Schulze et al., 2001; Popp et al., 2015). The formulation generally assumes that if the cavern pressure is near the local minimum stress, brine (or other fluid/gasses in the case of storage caverns) could infiltrate at grain boundaries and act as a pore pressure. This implicitely assumes pores can sufficiently be reached in a hydraulic sense, i.e., the Biot-coefficient is 1 under these stress conditions. The rock salt permeability is generally thought to change from ~10^{-21} m^2 to as much as 10^{-16} m^2 (e.g., Peach, 1991, Popp et al., 2001). The stress state at which changes in permeability start to occur remain ill-constraint.
In addition to better understand the relation between permeability and (effective) stress, a clear microphysical understanding of the process could help in the debate if permeation is distributed along the cavern roof/wall or if it has a tendency to localize to some extent (e.g., Urai et al., 2019). Localization may possibly follow intra-dome salt structures favoring higher permeation rates such as potentially: anhydrite layers, fine-grained salt, or salt with a relatively high insoluble content. Microstructures indicate that both diffuse dilatancy and hydrofracturing can take place under very low effective stress conditions in natural settings (Berest et al., 1999, Lux et al., 2005, Schoenherr et al., 2007). This includes conditions near lithostatic fluid pressure and a differential stress of a few MPa in the deep subsurface, conditions at which dissolution-precipitation processes (pressure solution creep) are expected to take place, which would induce healing of dilated grain boundaries and thus could counteract fluid infiltration into the grain boundaries (e.g., Houben et al, 2013, Chen et al., 2022). Healing effects may also point at a reversible permeability over time.
Moreover, even on the grain-size scale complicating factors may arise in the form of variability in the grain size presence of mega-grains (e.g., Kristallbrockensalz, Barabasch et al., 2023). Furthermore, flow along second phase lithologies, such as anhydrite layers with barrier properties, may allow the fluid pressure to rise sufficiently beyond the minimum principal stress leading to hydrofracturing (Wolters and Düsterloh, 2009). One, yet not well-investigated phenomenon is the permeation along or through microporous anhydrite, which could contribute to a heterogeneous permeation pattern due to large permeability differences (3-4 magnitudes) at a small scale. In general, porosity in low-permeable, crystalline anhydrite could form through hydration processes (Heeb et al., 2023), or by the co-existence of anhydrite with other sulfates such as polyhalite. Moreover, porosity could also be related to the inclusion of second phases such as talc in between the anhydrite grains (Keith et al., 2017).
The objective of this work was to gain better understanding of prevailing permeation processes by means of microstructural investigation of laboratory permeation tests conducted on heterogeneous natural rock salt samples. Such samples can lead to scattered data at similar experimental conditions due to the sample heterogeneity. At the same time such samples provide the best insight in how microphysical processes could work in natural settings, particularly considering insoluble content in the cavern wall. The permeation tests are aimed to assess the hydraulic properties as a function of the effective stress, with a specific emphasis on the influence of anhydrite inclusions and mega-grains on fluid flow within the salt matrix.

We aimed to test the following hypotheses on the permeation mechanisms (Figure 1):

1. Permeation along (micro-cracked) matrix halite grain boundary network
2. Permeation through transgranular micro-cracks of the mega-grains
3. Permeation along the interface of matrix halite with halite mega-grains and/or anhydrite bands
4. Permeation through porous anhydrite

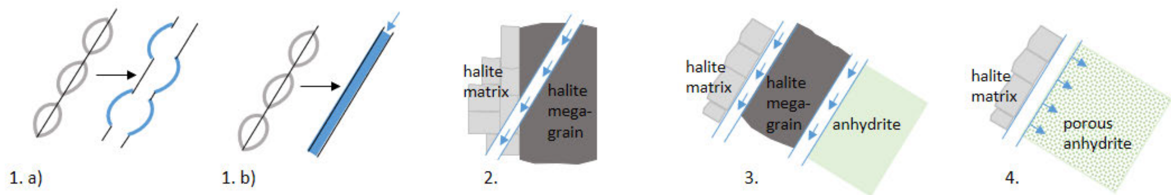

Figure 1. Schematic drawing of permeation mechanisms: 1a) permeation along dilatant grain bounadries, 1b) permeation through grain boundaries with connected pore fluid formed under differential stress (Drury and Urai, 1990), 2) permeation through transgranular cracks, 3) permeation along interfaces of fine-grained matrix halite with halite mega-grains/anhydrite, and 4) permeation through porous anhydrite inclusions.

Samples and Methods

Sample selection

Experiments were aimed to test the predicted effects of dilatancy by fluid-assisted microcracking and grain boundary dissolution-precipitation processes on permeation of heterogeneous salt around the caverns during operation and abandonment. Focus was on the effect of mineral heterogeneity on permeation, the evolution of fluid pressure and rate of permeation, to characterize the dilatancy and change in grain boundary processes (dilatancy, recrystallization, re-sealing and pressure solution) during the permeation experiments.
Sample selection of heterogeneous salt aimed was based onto test the hypotheses regarding the permeation behavior as stated above (Figure 1). Accordingly, samples were selected to allow testing of the different hypotheses by placing a mini-cavern at distinct locations within the core piece (Figure 3). Finally, based on the results from the micro-CT analysis (refer to the Results section) conducted on the initial core pieces, six samples were selected for the permeation tests (see Table 1).
The rock salt examined originates from 'Kristallbrockensalz' a renowned salt tectonite located in Zechstein II characterized by subvertical layering within the salt dome. Core inspection together with microstructural investigations reveal three key components: first, mega-grains of halite (Kristallbrocken), reaching decimeter lengths and up to 2 cm in thickness; second, a fine-grained halite matrix; and third, thin layers of fine-grained anhydrite folded and boudinaged, measuring a few millimetres in thickness. The mega-grains align subparallel to the bedding, while the halite matrix constitutes a variable portion of the rock. Notably, we observed closely packed, impermeable grain boundaries hosting equilibrated micropore arrays of fluid inclusions within the halite fraction. Halite mega-grains are characterized by presence of numerous second phase inclusions and have few healed, intergranular microcracks. The thin anhydrite bands and inclusions are usually interbedded with polyhalite and are often porous with some pores containing talc. Some grain boundaries showed dilation due to core damage.

Table 1. Overview samples and permeation processes.

Sample_ID	Tested Hypotheses #	Expected permeation processes	Hypotheses proven / not clearly proven #	Observed permeation processes
Perm2	1	Permeation along (micro-cracked) matrix halite grain boundary network	1 / -	Permeation through dilatant grain boundaries, some leaching
Perm3	2 & 3	Permeation through transgranular micro-cracks of the mega-grains / Permeation along the interface of matrix halite with halite mega-grains and/or anhydrite bands	1 & 3 / 2	Permeation along interface at megagrain- halite matrix and permeation through dilatant grain boundaries
Perm6	1 & 4	Permeation along (micro-cracked) matrix halite grain boundary network / Permeation through porous anhydrite	1 / 4	Permeation through dilatant grain boundaries
Perm4	3 & 4	Permeation along the interface of matrix halite with anhydrite bands / Permeation through porous anhydrite	3 / 4	Permeation along fractures at megagrain-matrix/anhydrite interface
Perm5	3 & 4	Permeation along the interface of matrix halite with anhydrite bands / Permeation through porous anhydrite	1 & 4 / 3	Permeation through porous anhydrite and dilatant grain boundaries
Perm8	2&3	Permeation through transgranular micro-cracks of the mega-grains / Permeation along the interface of matrix halite with halite mega-grains and/or anhydrite bands	3 / 4	Permeation along dilatant mega-grain/matrix halite/anhydrite interface

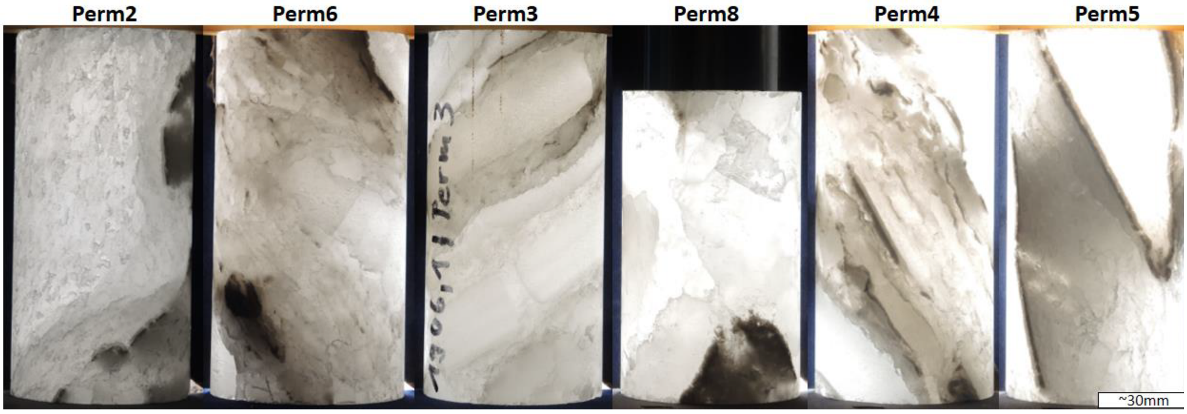

Figure 2. Transmitted light photographs of the selected core pieces with various content of halite mega-grains, matrix halite, and thin anhydrite bands and dust.

Permeation tests

Permeation tests were conducted utilizing hydraulic creep apparatuses equipped with a triaxial cell, facilitating controlled experimentation (Figure 4). The setup largely follows the setup as presented in Popp et al.,2015, with two key differences: 1) the samples are subjected to a relatively small differential stress to simulate a non-isotropic stress state at a cavern wall; and 2) instead of an inert gas the experiments are conducted using saturated brine.

We used cylindrical samples, measuring approximately 60 mm in diameter and 120 mm in length, were enveloped in rubber jackets to isolate pore pressure in the sample from the hydraulic oil used for confining pressure. Throughout the experiment samples are kept at 40 °C +/- 0.2 (104 °F +/- 0.36). Prior calibration of the temperature profile along the central axis revealed the constant temperature over the sample space.

The radial stress was maintained at 15 MPa (2175 psi) throughout the experiments. At the start of each experiment run, samples were subjected to an isostatic stress state to allow for compaction, i.e. a phase where any damage due to core preparation could heal. After this stage the axial stress was increased by 1 MPa (145 psi). Samples were subjected to this differential stress for the remainder of the experiment. Permeation tests spanned a duration of 30-50 days per experiment. During this period the axial displacement was logged to build up a stress strain curve as well, but is beyond the scope of this work. Moreover, the duration of the test was likely not enough to achieve a steady-state strain rate under these experimental conditions.

A small injection chamber, isolated from the rest of the sample, was prepared within each specimen. A 3 mm-diameter borehole was drilled into the sample and a thin metal hollow rod was cemented in place using epoxy. Subsequently using a smaller diameter drill the epoxy was drilled out through the rod and into the rock salt sample for a couple of millimeters, forming a miniature scale cavern (mini-cavern). Brine injection into this mini-cavern induced radial flow through the sample when permeation occurs. In such case brine could flow out of the apparatus via a porous mesh that is placed in between the rubber jacket and the rock sample, which allows for a hydraulic connection to the downstream part via a sintered filter plate between the sample and the lower piston of the apparatus.

The injection of brine on the upstream part was achieved using a Quizix® syringe pump and in some cases an equivalent system. This ensured a controlled fluid pressure or pressure-ramp, adjusting flowrates accordingly. Moreover, the pump could be programmed to stop automatically if the resulting flowrate was too high, i.e., a breakdown event. When this event occurred, the pump set the flowrate to zero but maintained recording the pressure, such that the pressure decay after a potential breakthrough event could be monitored.

To make sure the inflowing brine remained saturated, a small reservoir containing salt powder was strategically positioned atop each sample. Brine traversed this reservoir before entering the injection chamber, ensuring consistent saturation levels. This methodology allowed for the systematic investigation of permeation behavior under controlled conditions, providing valuable insights into fluid flow dynamics within the samples. Real-time data plotting facilitated prompt responses to any unexpected occurrences. This dynamic approach ensured efficient management of experimental conditions and enhanced the reliability of the results obtained.

Upon detection of a breakthrough of brine through the sample, typically expected at high injection pressures, injection operations were promptly halted automatically. This pause allowed the sample to undergo a potential healing process, possibly facilitating the closure of the breakthrough fracture within a time-window of typically a couple of days. Subsequently, in some experiments fluid pressure was increased again to facilitate further breakthrough, enabling comprehensive examination of the permeation process under varying conditions. This systematic approach ensured thorough exploration of sample behavior and provided valuable insights into the mechanics of fluid flow within the tested specimens.

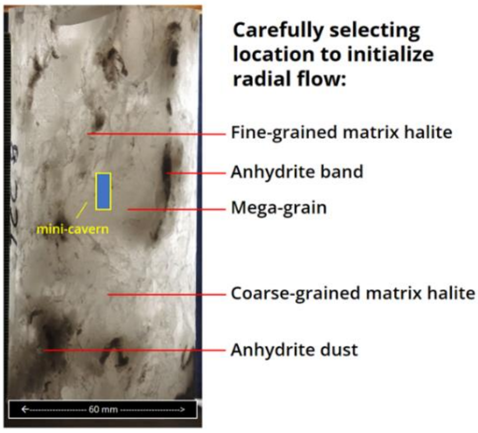

Figure 3. Generic example showing selection of location for preparation of the mini-cavern in heterogeneous rock salt.

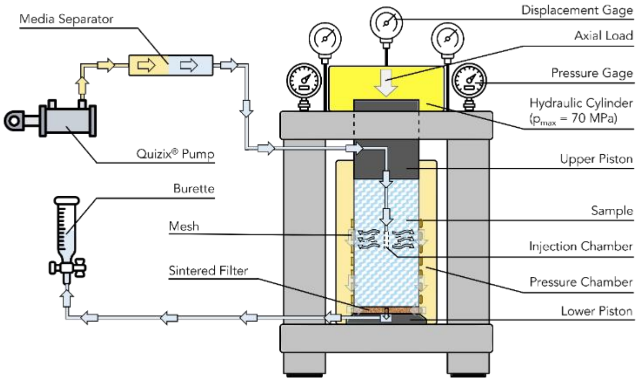

Figure 4. Technical drawing setup permeation device. Arrows indicate the flow direction of the brine used as the flow medium.

Microstructural analysis

All permeated samples underwent 3D scanning using a Nikon METRIS 3 X-TEK XT H 320 LC micro-CT scanner. Voxel resolution was determined by sample size, approximately 1/1000 of the field of view, resulting in voxel sizes ranging from 41 to 77µm. Visualizing the features of interest both before and after permeation involves addressing significant radial gradients in the data. To achieve this, contrast enhancement techniques were applied to improve the identification of fractures and anhydrite. Subsequently, segmentation techniques including 3D filtering, local thresholding, and the removal of small, unoriented noise were employed to delineate tubing, mini-caverns, fractures, and anhydrite. This facilitated the determination of their fractions and visualization of their interaction.
Following micro-CT scanning, the interior of the core pieces underwent impregnation with blue-dyed, low-viscosity resin under vacuum, utilizing existing tubing to highlight flow paths in most of the permeated samples. Thereafter, the sample material was prepared for further microstructural analysis by halving resin-impregnated sample cylinders parallel to the long axis. The selection of sections for cutting was precisely determined based on micro-CT scans.
The subsequent microstructural examination followed a strategic approach:
i) High-resolution flatbed scans in transmitted light were employed to study the overall microstructure of the cut faces of the samples and thin sections, with a pixel size of 5.3 µm. These scans were also utilized to select sub-samples for Optical Microscopy (OM) and Scanning Electron Microscopy (SEM) imaging.
ii) OM was conducted in both reflected and transmitted light using a Zeiss Axioscan 7 microscope equipped with an xyz-scanning stage. Magnifications of 25x, 50x, and 100x were employed, yielding micrographs with pixel sizes of 3.45 µm, 1.38 µm, and 0.69 µm, respectively. Single images and stitched mosaics were acquired for further qualitative and semi-quantitative microstructural analyses. Hue values of transmitted light flatbed scan images, as well as micrographs acquired using the optical microscope, were adjusted to enhance differentiation between the blue resin utilized for ex-situ visualization of flow paths and the resin employed for thin section preparation. Consequently, the blue resin appears magenta in the micrographs, while the resin used for thin section preparation appears greenish.
iii) Sub-samples, such as BIB (Broad Ion Beam) polished cross-sections (e.g., Desbois et al., 2013), and thin sections were imaged in a Zeiss Supra 55 field emission Scanning Electron Microscope (SEM). Simultaneously acquired Energy Dispersive Spectroscopy (EDS) was employed to trace resin inside the pore space to visualize preserved permeation pathways.

Results

Permeation tests

The permeation experiment for Perm2 (Figure 5a) indicates several breakthroughs. The first breakthrough was observed at a brine pressure (pBrine) of 15.2 MPa- (2205 psi) after 26 days, followed by a second breakthrough at 11.7 MPa (1697 psi), and a third at 15 MPa (2176 psi). Visual inspection of the deformed sample did not reveal a clear indication of where the breakthrough occurred. Comparing this with microscopic analyses, we presume that permeation along grain boundaries would have ultimately led to the breakthrough. Experiment Perm6 demonstrated no breakthrough despite incrementally increasing injection pressure up to 15.5 MPa (2248 psi). Only slight variations in flow rate were observed throughout this phase (Figure 5b). Sample Perm3 indicated no breakthrough after four days under isostatic conditions; only after increasing the pBrine to 16.4 MPa (2379 psi) did a breakthrough occur. After a resting phase of 14 days, the pBrine was decreased to 2 MPa (290 psi) without any further breakthrough, indicating healing processes within the sample (Figure 5c).
After step-wise and progressively increasing ramps of 2 MPa/d (290 psi/d) and 0.4 MPa/d (58 psi/d), the injection pressure was held constant at 20 MPa during testing of specimen Perm8 (Figure 5d). This specimen contains almost no impurities but has an intact Halite matrix. Since no breakthrough of the brine was evident after a period of 11 days at a constant injection pressure of 20 MPa (2900 psi), the pressure was slowly increased until a breakthrough could be observed at 20.5 MPa (day 48), dropping to 17.4 MPa after the injection system was stopped for the remaining five days of the experiment.
Under (quasi) isostatic conditions, increasing the injection pBrine to 12 MPa (1740 psi) at a rate of 2 MPa/d (290 psi/d) and keeping it constant resulted in relatively high flow rates in sample Perm4 (Figure 5e). Decreasing the injection pressure to 8 MPa (1160 psi) and holding it constant for four days led to some healing as the flow rate dropped slightly. However, subsequently increasing the injection pressure to its ultimate value of 15.2 MPa (2205 psi with a ramp of 0.4 MPa/d or 58 psi/d) resulted in an increasing flow rate, triggering the pump alarm and stopping pressure control. Stopping the injection for 13 days yielded a final injection pressure of 9.7 MPa (1407 psi).
Sample Perm5 (Figure 5f) displayed somewhat unique behavior. After increasing the injection pressure to 12 MPa (1740 psi) and 16 MPa (= σ_1, 2321 psi) at rates of 2 MPa/d and 0.4 MPa/d respectively (290 psi/d and 58 psi/d), no breakthrough of the brine could be observed for three days. Decreasing the injection pressure to 12 MPa (1740 psi), holding it constant for four days, and subsequently increasing again to 16 MPa (2321 psi), led to a breakthrough and pressure drop after holding it constant for three days, possibly due to static fatigue of the sample throughout the experimental duration. Ultimately, an injection pressure of 9.7 MPa (1407 psi) was measured at the end of the test.

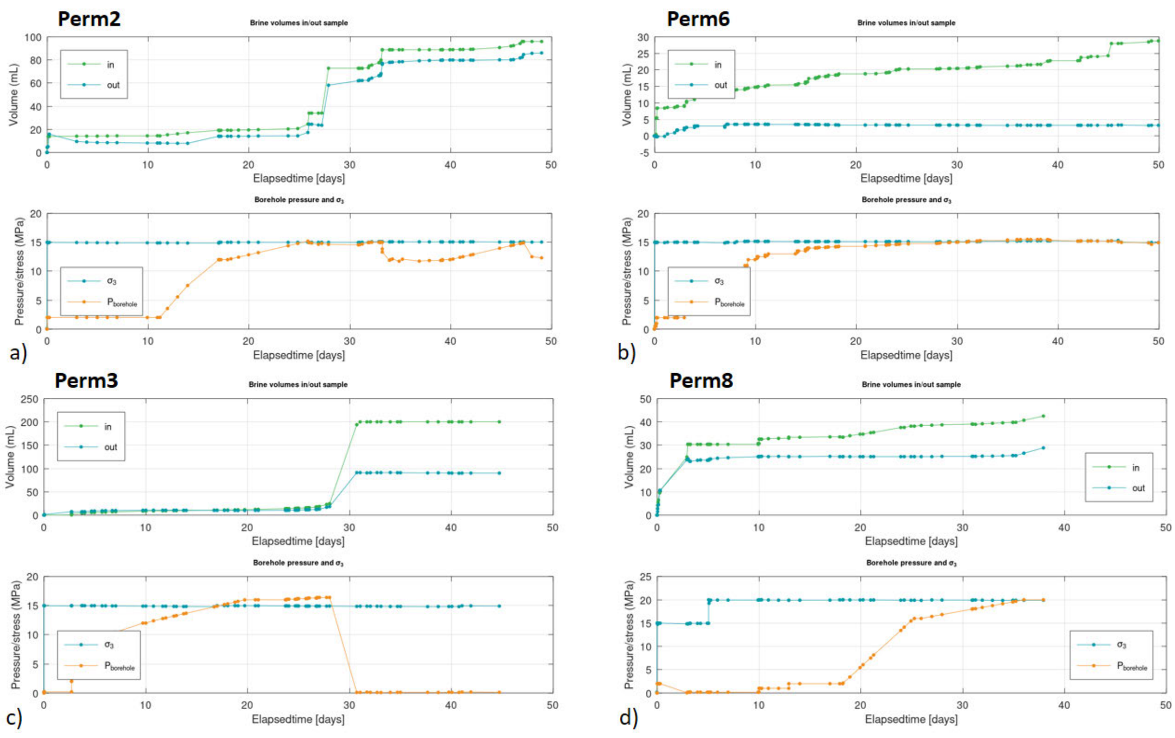

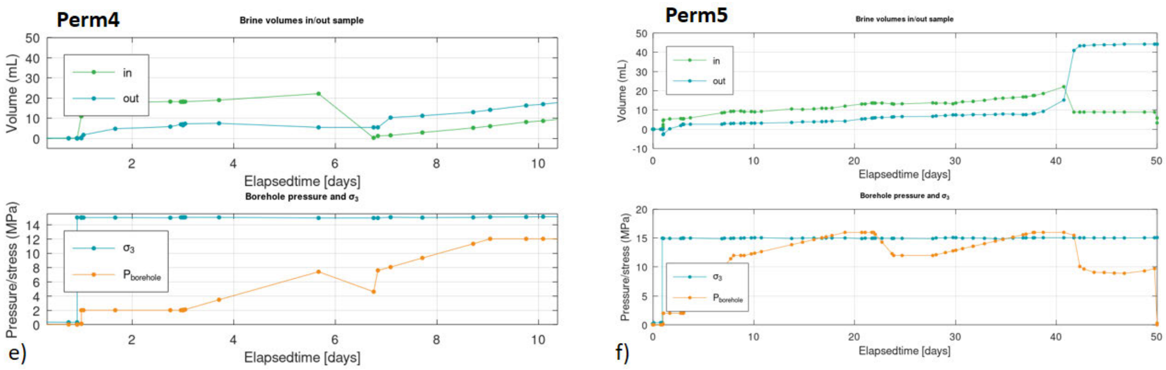

Figure 5. Results of permeation tests. Please refer to the text for the description. Each test, labelled with a), b) etc. has two panels. Upper panel displays volumes of brine going in (green) and out (blue) of the sample space. Lower panels display the mini-cavern / borehole pressure (orange) and the confining pressure (blue) as reference

Microstructural investigation

For a clearer illustration of the results, we combined the permeated samples that exhibited a similar distribution of the phases, including the polycrystalline matrix, halite mega grain interface, and porous anhydrite (Table 1, Figure 1, Figure 3 and Figure 6). Consequently, these samples were chosen to demonstrate similar permeation processes:

a) Samples Perm2 and Perm6 were primarily selected to validate hypothesis 1, focusing on permeation through the matrix-halite grain boundary network.
b) Permeation through samples Perm3 and Perm8 was conducted to primarily test hypotheses 2 and 3, exploring potential permeation through transgranular micro-cracks of the mega-grains, as well as permeation along the interface of matrix halite with halite mega-grains and/or anhydrite bands.
c) Samples Perm4 and Perm5 were chosen to examine the influence of abundant porous anhydrite on permeation behaviour, in line with hypotheses 3 and 4, considering possible permeation along the interface of matrix halite with anhydrite bands and/or permeation through porous anhydrite.\

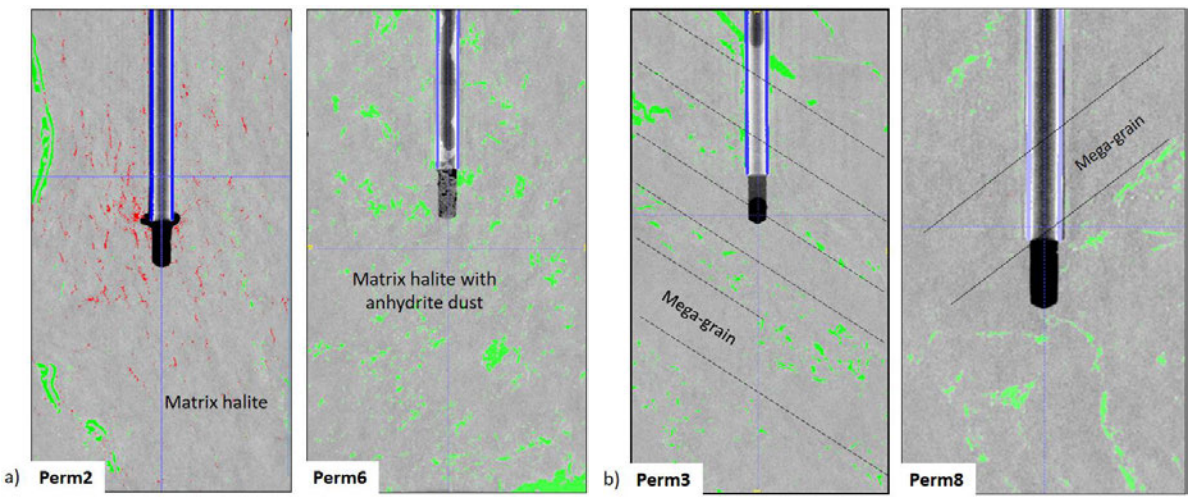

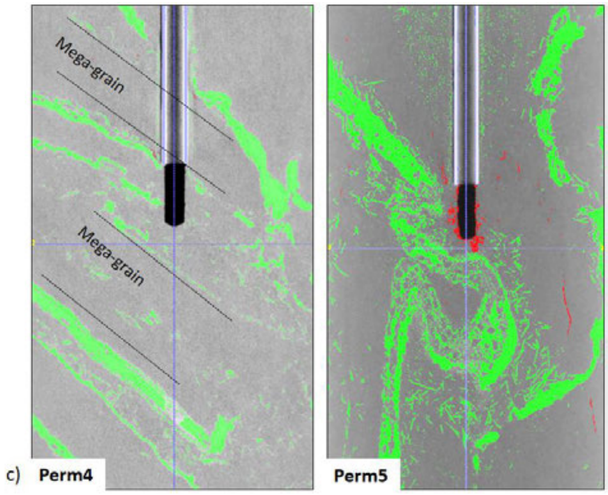

Figure 6. Combining samples with similar structure and phase distribution to test the various hypothesized permeation processes: a) permeation trough dilatant grain boundaries in polycrystalline halite matrix. b) permeation along interface of polycrystalline halite matrix to halite mega grain. c) permeation through porous anhydrite. Segmentation result for anhydrite displayed in green and segmentation of the fracture space displayed in red, both superimposed on filtered CT-Data.

Permeation through the matrix halite grain boundary network (a)

Core piece Perm2 predominantly consists of a fine-grained polycrystalline matrix of halite, with minor halite mega-grains, and approximately 1.54 vol% of anhydrite (Figure 2), manifested as a few millimetres thick bent and ruptured band located at the opposite edge of the test cylinder. A micro-CT scan (Figure 7) was conducted both before and after the Perm2 permeation experiment. The tubing was positioned within the homogeneous fabric to facilitate the formation of the mini-cavern at the sample's centre. Prior to the permeation experiment, the anhydrite content was segmented at 1.54 vol%, while the fracture space was segmented at 0.22 vol%. Post-permeation, the segmented anhydrite content decreased to 1.05 vol%, while the fracture space increased to 0.44 vol%. The highest fracture density was observed in close proximity to the mini-cavern, gradually decreasing towards the outer edges of the core piece (Figure 7). The shape and orientation of the identified fracture space follow the orientation of the elongated matrix grains, indicating permeation along a dilatant grain boundary network. At the tubing, the cavern bulges, likely due to late-stage leaching processes associated with temporary undersaturation of the brine as a result of high flow rates towards the end of the test. This is also associated with some wormhole-like dissolution pathways that taper-out a few millimetres away from the cavern.

In transmitted light, we observed impregnation of the grain surfaces with blue-dyed resin in the vicinity of the mini-cavern (Figure 8). Nonetheless, this feature does not extend uniformly throughout the core piece to the same degree as observed in the micro-CT images, presumably due to the wetting properties of the resin in relation to the vacuum pressure used for impregnation, which did not allow further penetration of the dilatant grain boundaries in the far field.

When comparing the grain boundaries of a non-treated twin sample with the permeated sample in the optical micrographs (see Figure 9), we noted only minor modifications in the grain boundary structure for boundaries oriented perpendicular to the axial load direction. These boundaries typically displayed remnants of isolated fluid inclusions. However, grain boundaries parallel to the axial load direction clearly demonstrated dilatancy, as evidenced by resin impregnation and alterations in fluid inclusion imprints, resulting in a more irregular and patchy surface morphology. This observation was confirmed in the SEM (Figure 9d), where we identified dilated grain boundary segments containing resin, alongside closed grain boundary segments occasionally showing efflorescence, indicating the presence of grain boundary fluids prior to thin section preparation (Schenk and Urai, 2004).

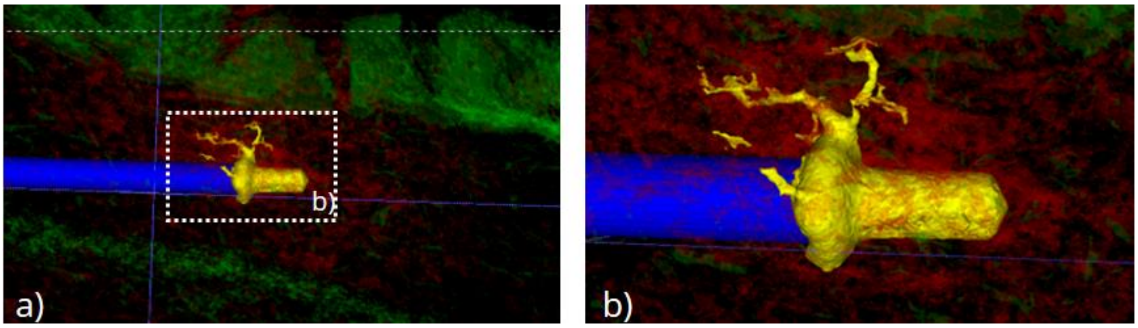

Figure 7. 3D micro-CT Results for Perm2: a) 3D visualization showcasing segmented phases, featuring the miniature cavern highlighted in yellow, with anhydrite represented in green, and fracture space displazed in red. b) Close-up 3D visualization highlighting the mini-cavern in yellow. For a detailed description of the images, please consult the accompanying text.

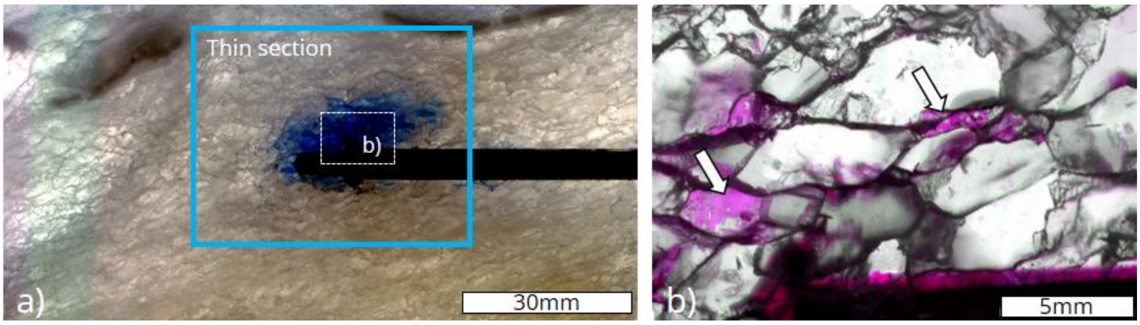

Figure 8. a) A slab prepared at the center of core piece Perm2 was imaged in transmitted light. Blue dyed resin was utilized to visualize the permeation pathway ex-situ. b) A thin section micrograph captured in transmitted light illustrates resin impregnated grain boundaries in the vicinity of the mini-cavern.

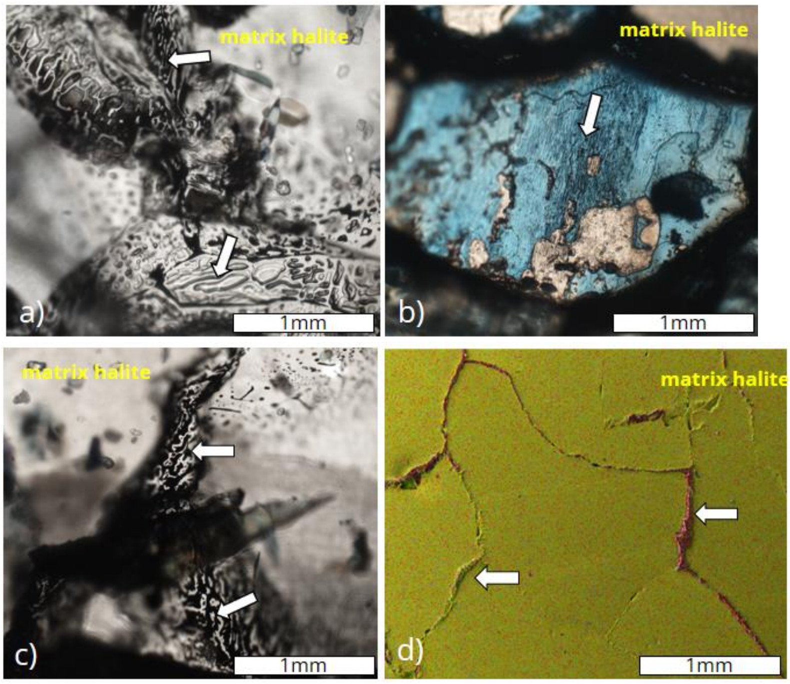

Figure 9. a) thin section micrograph of an untreated twin sample imaged in transmitted light showing grain boundary structure with numerous fluid inclusions, b) thin section micrograph imaged in transmitted light showing dilatant grain boundary, impregnated with resin, oriented parallel to the axial load direction. c) thin section micrograph imaged in transmitted light showing tight grain boundary with fluid inclusions, oriented perpendicular to the axial load direction, d) SEM/EDS micrograph showing resin inside grain boundaries. See the accompanying text for further explanation.

Core piece Perm6 was selected due to its mylonitic fabric and the relatively high variability in halite matrix grain size and shape. Anhydrite is discernible as nodules and minor anhydrite dust (see Figure 2), while halite mega-grains are situated in the middle portion of the chosen core piece. The tubing was positioned within the coarse-grained polycrystalline halite matrix, with adjacent anhydrite layers.
Micro-CT data reveals a segmented anhydrite content of 6.05 vol% and segmented fracture space of 0.49 vol% before permeation (see Figure 10). Subsequently, the segmented anhydrite content decreased to 4.90 vol%, with no segmented fracture space at a voxel resolution of 41 µm.
Results obtained from OM and SEM indicate dyed resin impregnating along grain boundaries, effectively preserving fluid imprints. However, only minor impregnation was observable in the scanned thin section (refer to Figure 11 and Figure 12). Upon comparing the grain boundaries of the tested samples with those of twin samples in their initial state, noticeable alterations are observed in the grain boundaries oriented parallel to the axial load direction, similar to sample Perm2.

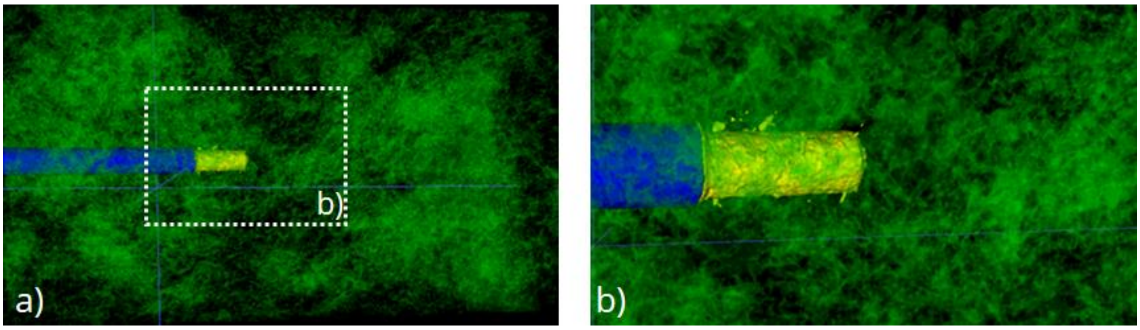

Figure 10. 3D micro-CT Results for Perm6: a) 3D visualization showing segmented phases, including the miniature cavern highlighted in yellow, with anhydrite represented in green, and fracture space displayed in red, b) close-up 3D visualization. For a detailed description of the images, please consult the accompanying text.

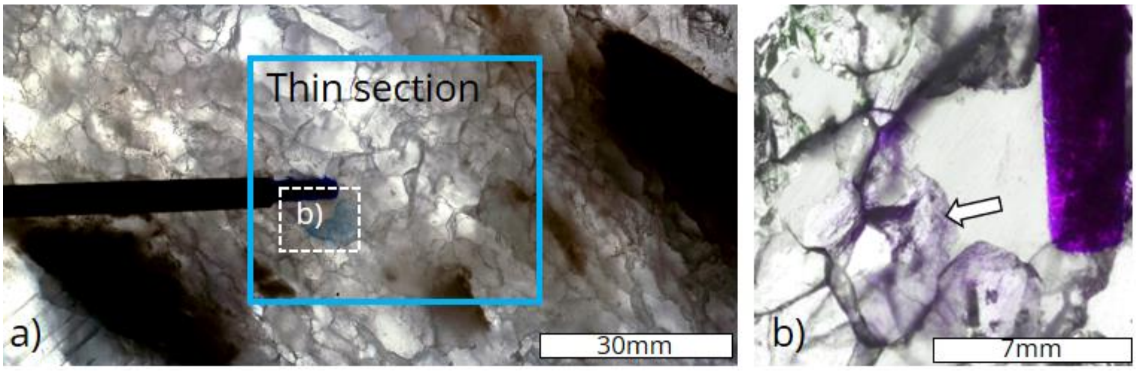

Figure 11. a) A slab prepared at the center of core piece Perm6 was imaged in transmitted light. Blue dyed resin was utilized to visualize the permeation pathway ex-situ. b) A thin section micrograph captured in transmitted light illustrates resin impregnated grain boundaries in the vicinity of the mini-cavern.

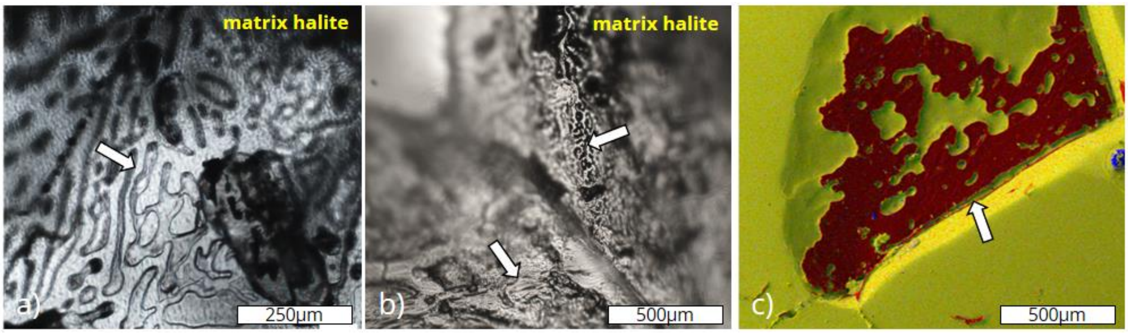

Figure 12. a) thin section micrograph of an untreated twin sample imaged in transmitted light showing grain boundary structure with numerous fluid inclusions, b) thin section micrograph imaged in transmitted light showing tight grain boundary with fluid inclusions, oriented perpendicular to the axial load direction, c) SEM/EDS micrograph showing, resin (C, red color) covered grain surface oriented parallel to the axial load direction .

Permeation through transgranular micro-cracks and along phase interfaces (b)

Sample Perm3 primarily comprises halite mega-grains with thin layers of anhydrite and matrix halite in between. The anhydrite layers predominantly occur at the interfaces of halite mega-grains. This sample was selected for its high content of halite mega-grains (refer to Figure 2). The interface between matrix halite and a halite mega-grain was chosen as the tubing and mini-cavern placement site.

Analysis of the micro-CT data yielded a fraction of 2.57 vol% anhydrite and 0.40 vol% fracture space before permeation (see Figure 13). Following permeation, no fracture space was detected, and the anhydrite content remained at 2.58 vol%, indicating consistent results and good comparability of CT scans and segmentation before and after permeation. The mega-grain exhibits transgranular micro-fractures oriented perpendicular to the major axis of the mega-grain and inclined approximately 30 degrees from the σ1 direction.

Optical microscopy using reflected and transmitted light revealed only minor visible intrusion of the blue-dyed resin into the matrix halite grain boundaries (see Figure 14 and Figure 15). Upon comparing the interface of the matrix grains with the mega-grains near the cavern in the OM, a modification of the grain boundary structure is clearly evident in the form of widespread dilatant zones with only a few remaining grain-to-grain contacts.

SEM investigation showed the majority of impregnated grain boundaries in the polycrystalline halite above the mega-grain. However, high-resolution SEM on the etched thin section surface clearly depicted resin impregnation at the interface of the mega-grain with the polycrystalline halite matrix grains (see Figure 15). Additionally, some impregnations were also detected below the mega-grains, indicating permeability of the mega-grain to the dyed resin.

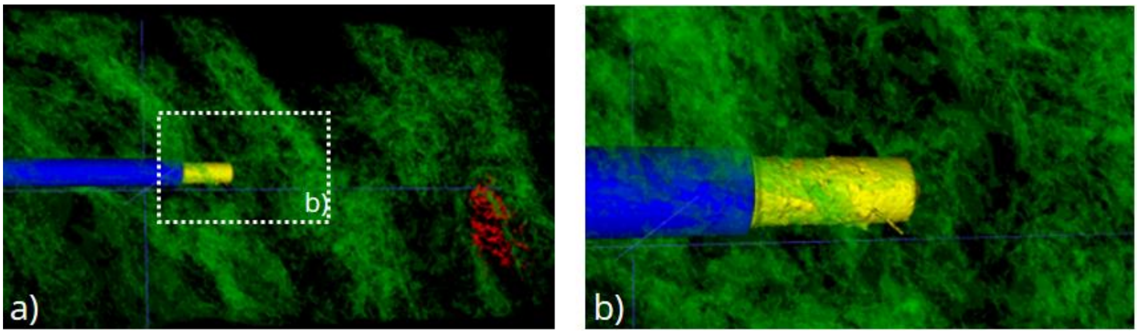

Figure 13. 3D micro-CT Results for Perm 3: a) 3D visualization showcasing segmented phases, featuring the mini-cavern highlighted in yellow, with anhydrite represented in green, and fracture space delineated in red, b) close-up 3D visualization. For a detailed description of the images, please consult the accompanying text.

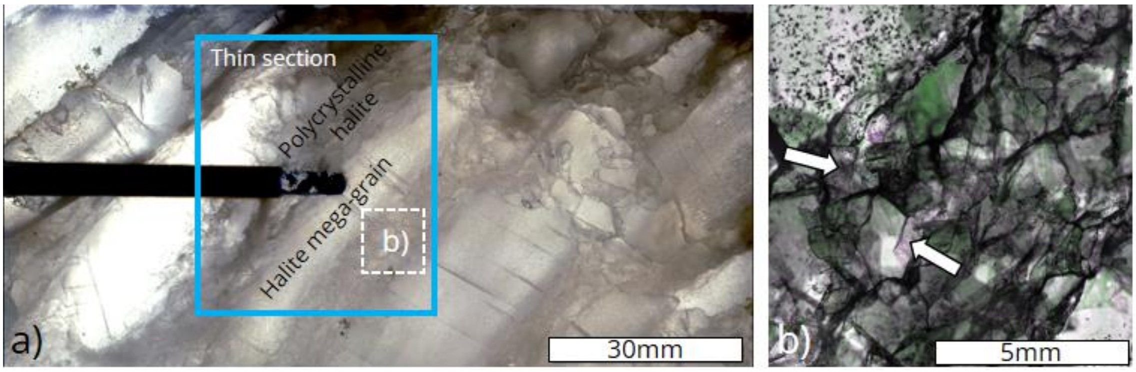

Figure 14. a) A slab prepared at the center of core piece Perm3 was imaged in transmitted light. Blue dyed resin was utilized to visualize the permeation pathway ex-situ. b) A thin section micrograph captured in transmitted light illustrates resin impregnated grain boundaries in the vicinity of the mini-cavern.

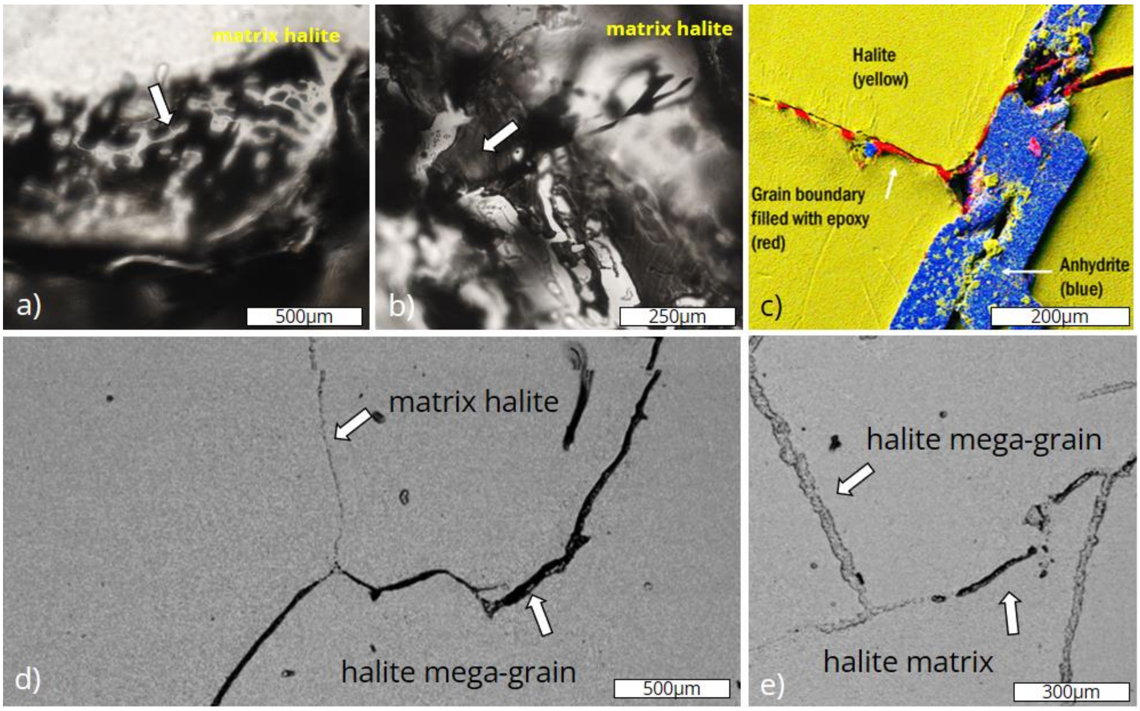

Figure 15. a) thin section micrograph of an untreated twin sample imaged in transmitted light showing interface of matrix halite with a mega-grain, b) thin section micrograph of sample Perm3 imaged in transmitted light showing dilatant interface if matrix halite with a mega-grain, c) SEM/EDS micrograph showing, resin (C, red color) inside grain boundary oriented parallel to σ1 cross-cutting an anhydrite grain, d) matrix halite/mega-grain interface cross-section imaged in the SEM filled with resin (black diagonal line), matrix halite grain boundary (upper arrow) shows efflorescence, f) matrix halite/mega-grain interface cross-section imaged in the SEM filled with resin (lower arrow), matrix halite grain boundary (upper arrow) shows efflorescence.

Sample Perm8 primarily contains mega-grains interspersed with matrix halite bands, with a thin anhydrite band located at the side of the core piece. The polycrystalline matrix halite exhibits notable anhydrite dust (refer to Figure 2). Before permeation, Perm8 was CT-scanned, revealing a significant number of fractures, some with relatively large apertures spanning a few voxels. Segmentation of the post-processed data yielded a 2.2% anhydrite fraction and 0.6% fracture space.

Post-permeation, only 0.01% of fracture space was identified from the post-processed data, primarily in close proximity to the mini-cavern. The anhydrite fraction remained virtually unchanged after segmentation (see Figure 16). The blue-dyed resin is prominently visible at the interface of the mega-grain and the very thin anhydrite laminae (refer to Figure 17 and Figure 18), indicating preferential permeation along the interface. Additionally, the anhydrite was locally impregnated with resin.

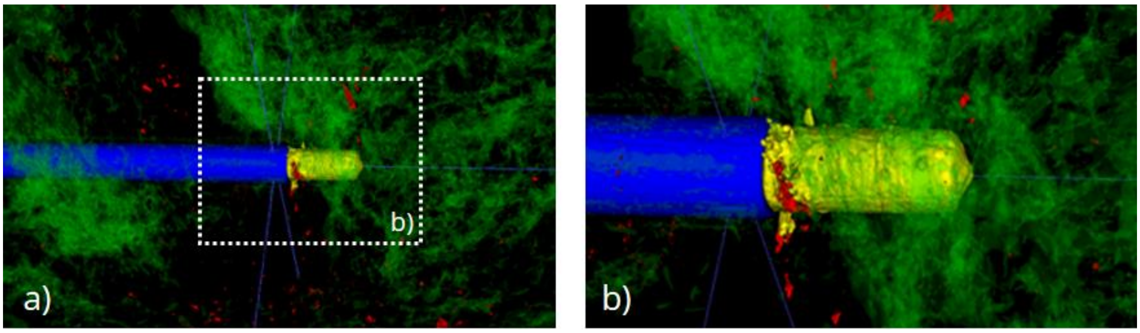

Figure 16. 3D micro-CT Results for Perm8: a) 3D visualization showing segmented phases, including the mini-cavern highlighted in yellow, with anhydrite represented in green, and fracture space delineated in red, b) close-up 3D visualization. For a detailed description of the images, please consult the accompanying text.

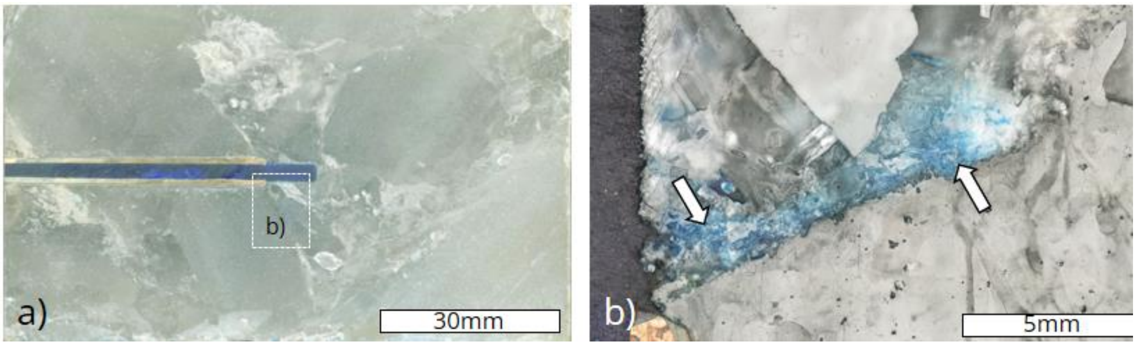

Figure 17. a) A slab prepared at the center of core piece Perm8 was imaged in transmitted light. Blue dyed resin was utilized to visualize the permeation pathway ex-situ. b) A thin section micrograph captured in reflected light illustrates resin impregnated grain phase contacts of matrix halite with a mega-grain associated with anhydrite in the vicinity of the mini-cavern.

Permeation through/along porous anhydrite (c)

Sample Perm4 exhibits a significant presence of mega-grains and anhydrite, closely associated with each other, although the coarse-grained polycrystalline halite constitutes the primary fraction. These features are distinctly visible in both the untreated and permeated core (refer to Figure 2 and Figure 6). Following the permeation experiment, micro-CT scans revealed the clear inception of a fracture through the middle of the mini-cavern along the mega-grain/anhydrite interface (see Figure 18). Despite its small aperture, further examination in the micro-CT scan revealed a few larger cavities deeper within the sample. The quantity of anhydrite was relatively high, approximately 8.9%, as determined through image segmentation. Fracture space was minimal, nearly absent, and primarily localized near the mini-cavern.

Optical microscopy and scanning SEM analyses of the slabs provided clear evidence of blue-dyed resin impregnation at the contact points between anhydrite and mega-grains, traversing the mini-cavern (refer to Figure 19 and Figure 20). This impregnation occurred through an approximately 100 µm wide fracture along the anhydrite/matrix halite interface. Additionally, transmitted light OM revealed that the blue-dyed resin penetrated the matrix halite grain boundaries approximately 20 mm away from the mini-cavern.

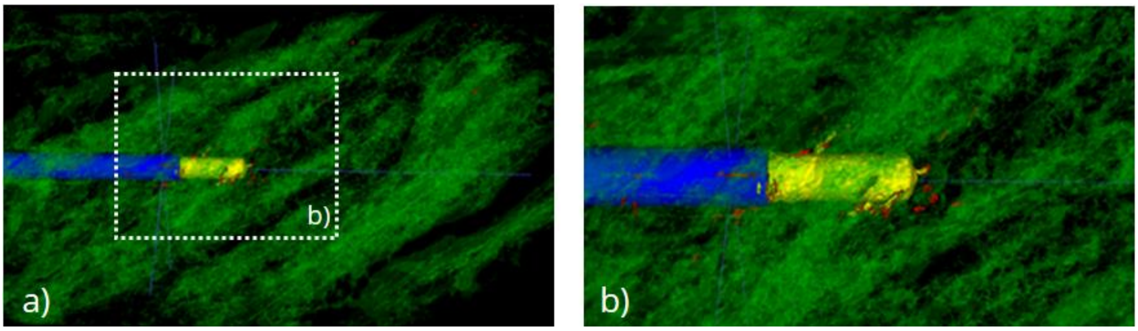

Figure 18. 3D micro-CT Results for Perm4: a) 3D visualization showing segmented phases, including the mini-cavern highlighted in yellow, with anhydrite represented in green, and fracture space delineated in red, b) close-up 3D visualization. For a detailed description of the images, please consult the accompanying text.

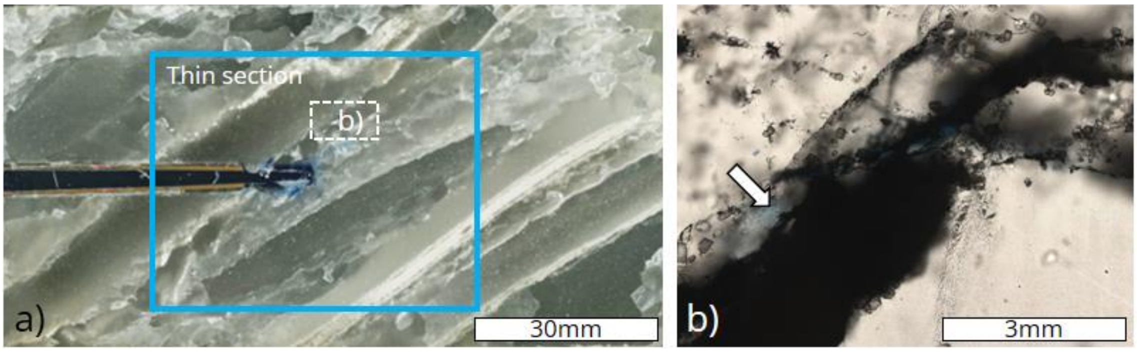

Figure 19. a) A slab prepared at the center of core piece Perm4 was imaged in transmitted light. Blue dyed resin was utilized to visualize the permeation pathway ex-situ. b) A thin section micrograph captured in transmitted light illustrates resin impregnated grain boundaries in the vicinity of the mini-cavern.

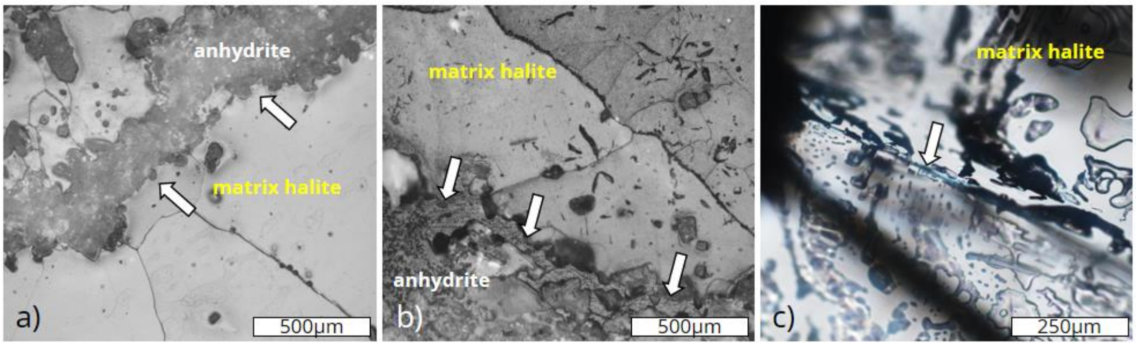

Figure 20. a) thin section micrograph of an untreated twin sample imaged in reflected light showing intact anhydrite/halite interface, b) thin section micrograph imaged in reflected showing crack along anhydrite/halite interface, c) thin section micrograph imaged in transmitted light showing resin impregnated grain boundary within matrix halite.

Sample Perm5 contains parts of bent mega-grains bounded by folded anhydrite laminae, while the matrix consists of relatively coarse-grained, polycrystalline halite. The micro-CT scan of Perm5 after permeation reveals the mini-cavern situated near the flank of an anhydrite microfold (see Figure 21). Pore space was likely created adjacent to the mini-cavern, with a few fractures parallel to the core axes present, primarily located off-center and seemingly disconnected at the achieved resolution. The amount of anhydrite is estimated to be approximately 10.8%, while the pore space (including fractures) is around 0.1%, based on 3D image segmentation of the post-processed data.
In Figure 22, the halved permeated core after resin impregnation clearly indicates resin intrusion in the anhydrite laminae. At higher resolution, the blue dye appears mainly localized within the anhydrite or restricted very close to the edge of the mini-cavern, consistent with the pore space segmented from the micro-CT scan. The resin-impregnated anhydrite was subsampled, BIB-polished, and investigated in the SEM, illustrating that a significant portion of the anhydrite was porous and filled with resin (refer to Figure 23). This porosity in the anhydrite band is believed to have developed through leaching of the interbedded porous polyhalite, which is visible in the untreated twin sample using BIB-SEM (see Figure 23).

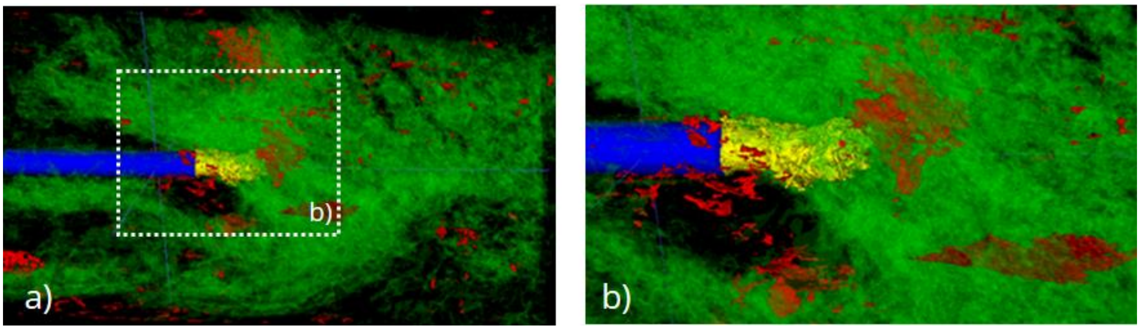

Figure 21. 3D micro-CT Results for Perm 5: a) 3D visualization showing segmented phases, including the mini-cavern highlighted in yellow, with anhydrite represented in green, and fracture space delineated in red, b) Close-up 3D visualization. For a detailed description of the images, please consult the accompanying text.

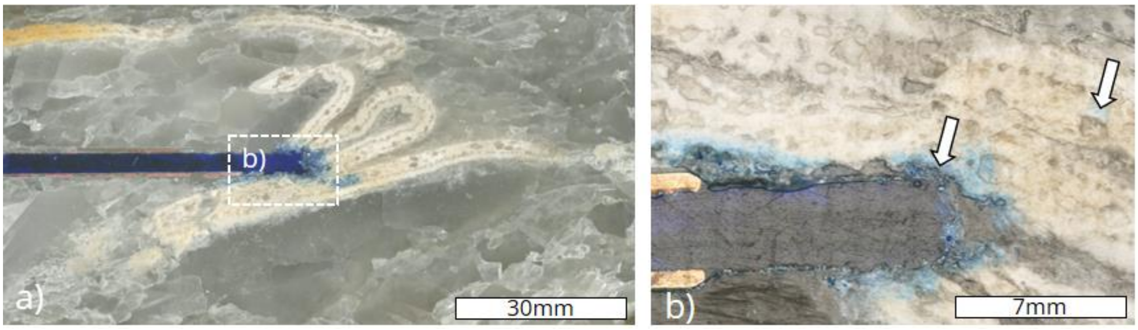

Figure 22. a) A slab prepared at the center of core piece Perm5 was imaged in transmitted light. Blue dyed resin was used to visualize the permeation pathway ex-situ. b) A thin section micrograph captured in reflected light illustrates resin impregnated porous anhydrite in the vicinity of the mini-cavern.

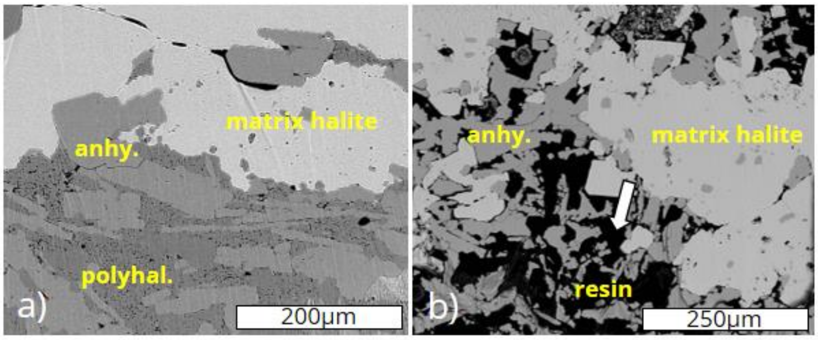

Figure 23. BIB-SEM micrographs showing a) twin sample with anhydrite containing polyhalite in contact with matrix halite and b) anhydrite with resin-filled (previously polyhalite) pore space in contact with matrix halite.

Discussion

The permeation experiment conducted on Perm2 revealed several breakthrough events. The first breakthrough occurred at a brine pressure (pBrine) of 15.2 MPa after 26 days, followed by a second breakthrough at a pBrine of 11.7 MPa, and a third at 15 MPa (see Figure 5). Microscopic analyses suggest that these breakthroughs likely transpired due to permeation along grain boundaries. Optical microscopy clearly depicts impregnation of dyed resin along the grain boundaries of the thin sections. These findings were corroborated by SEM images illustrating dilatant grain boundaries filled with blue-dyed resin, delineating flow paths.

Contrarily, the permeation experiment with Perm6 demonstrated no breakthrough despite incrementally increasing injection pressure up to pBrine 15.5 MPa. Throughout this phase, only slight variations in flow rate were observed (refer to Figure 5). We postulate that the coarser-grained halite matrix may be permeating along dilatant grain boundaries, potentially requiring more time to do so, and a breakthrough may have eventually occurred.

In the rather homogeneous samples, such as Perm2 and Perm6, which predominantly consist of matrix halite, we infer that the primary permeation process involves flow through continuously dilating grain boundaries (Berest et al., 1999, Lux et al., 2005). Grain boundary structures indicate that reactivation of continuous grain boundary fluid films was not actively contributing to this process (Urai et al., 2019). However, alterations were observed on the grain surfaces of the dilatant grain boundaries, typically oriented parallel to the axial load direction, which could be attributed to dissolution processes.
Experiment Perm3 initially showed no breakthrough after four days under isostatic conditions. Only after increasing the pressure to pBrine 16.4 MPa was a breakthrough observed. Following a resting phase of 14 days, the pressure was reduced to pBrine 2 MPa without further breakthrough, indicating some healing processes within the sample (see Figure 5). Permeation pathways were primarily traced at the interface of the mega-grain with the polycrystalline matrix halite, as well as along matrix halite grain boundaries, which were deemed less efficient as only minor resin impregnation was detected along these grain boundaries. Cracks in single crystals are thought to heal faster than grain boundaries, which supports this observation (Houben et al., 2013). Compared to the initial samples, microcracks within the mega-grains extended in both length, from intragranular to transgranular, and frequency, indicating microcracking within mega-grains due to the stress state in the sample. Microcracking of the matrix grain, however, was not observed.
In sample Perm8, dyed resin was prominently visible at the interface of a halite mega-grain with a thin anhydrite band. The sample was initially permeable at the start of the test, but presumably healed when subjected to higher confinement of 20 MPa (refer to Figure 5). Eventually, a clear breakthrough occurred when the fluid pressure exceeded the confining pressure. Permeation through sample Perm4 exhibited early leak-off, as depicted in Figure 5, but was intentionally healed thereafter. Subsequently, fracture closure was observed at approximately 10 MPa following the actual breakthrough. It is likely that permeation occurred along the fractures at the mega-grain/matrix halite/anhydrite interface, intersecting the mini-cavern. This inference is supported by the presence of apertures and blue resin observed using ex-situ microstructural analysis. Based on the results of the microstructural investigations, we infer that preferred permeation occurred along the mega-grain/anhydrite interface in samples Perm3, Perm4 and Perm8, pointing to the relevance to further study the interface strength of adjacent phases in heterogeneous rock salt as an input parameter for microscale permeation models (e.g., Chen et al. 2022).
In sample Perm5, leak-off was observed relatively early, occurring after 18 days, following which the sample healed again. Around day 39, another breakthrough occurred, preceded by "fracture closure" observed at approximately 9 MPa. Notably, the borehole pressure had to significantly overcome the σ_3 stress to initiate flow. This suggests that the tensile strength of the samples is relatively high, likely due to the presence of complex folded anhydrite laminae, which increases the overall bonding strength of the sample. Comparing the microstructures with the permeation experiment, we can infer that the anhydrite certainly contributed to accommodate space, although it likely only provided localized pathways for permeation, as resin impregnation was observed only locally and appeared to be related to preferential dissolution of the interbedded porous polyhalite. Subsequently, the porous anhydrite could have formed connecting bridges between dilatant grain boundaries, which closed and healed again after the experiment (Houben et al., 2013) as they are not visible in the planar BIB cross-section in the SEM. Since the connected porosity in the anhydrite was induced by the dissolution of the polyhalite, this feature is regarded as local and associated with experimental artifacts. It may not accurately reflect conditions found in natural prototypes, where undersaturation of the brine would not be anticipated.

The variability in the observed behavior in the samples in terms of the maximum pressure is too large to draw statistically valid conclusions on for example at what effective stress level the rock salt permeability starts to change. Thereby upscaling to assess at what level such an onset of permeation behavior occurs requires more tests when considering the experiment data alone. Given sample variability and heterogeneity this might not be a feasible approach. However, using the microstructural observations numerical models could be built to further explore the microphysical permeation behavior. In such models, heterogeneity could be systematically varied as well as the mechanical / hydraulical properties of salt-grain contacts, salt-grain/anhydrite/clay content contacts etc. In addition, “digital twins” of the samples could be built based on micro-CT 3D image volumes of actual samples. Using this approach, the outcome of laboratory tests and that of numerical approach can be compared. Such effort may also better reveal micro-scale differences in the stress state within the sample. For example, it could be the case that for some tests where high mini-cavern pressures were observed this pressure acted as a boundary condition stressing the rock salt at the mini-cavern wall to deform. Here the local stress state may have been elevated and thus locally a permeation threshold could have been higher.

Such an investigation should also look at the effect of the rate of which the pressure is increased. If the pressure is increased more slowly, there may have been enough time for the mini-cavern to deform plastically (dislocation creep / pressure solution creep). In our set of tests, the pressure rates were kept in a similar range as the focus was on the sample heterogeneity. We hypothesize that a slower pressure increase may show higher sustained mini-cavern pressures.
Furthermore, tests may be aided by the use of passive acoustic emission (AE) measurement systems, to address the distribution of cracking within the sample. This may help to identify where cracking occurred within the sample and where in relation to the central mini-cavern. Moreover, acoustic emission data could potentially also be used to better understanding of field microseismicity (e.g., Burlini et al., 2007, Bakker et al., 2016). It may be that permeation (inferred from cracking) started out distributed and eventually localizes to a fracturing event associated sudden pressure drop. Using AE the moment in time could be determined and helps to better understand pressure evolution.

Conclusions

Permeation tests conducted on heterogeneous rock salt provided microstructural evidence supporting hypotheses 1 and 3: permeation along the micro-cracked matrix halite grain boundary network and along the interface of matrix halite with halite mega-grains and/or anhydrite bands. The contribution of dissolution-precipitation was found to be of minor importance in this process. Pronounced hydrofracturing of intact halite grains, as posited by hypothesis 2, was not observed in the tests. Therefore, the extent of permeation along transgranular cracks could not be fully evaluated in this study. However, it is believed that transgranular cracks within halite mega-grains contribute to permeation, albeit to a lesser extent compared to permeation along phase interfaces and the present dilated grain boundaries. Permeation through porous anhydrite (hypothesis 4) was observed in the tested core pieces. However, it is thought to be related to experimental artifacts, particularly the preferential dissolution of associated polyhalite. This phenomenon is unlikely to scale with the conditions found in natural salt formations.
While further testing is required to better understand permeation behavior and its relation to effective stress, the combination of microstructural investigations with laboratory testing proved to be a valuable addition. Microstructural evidence provides a better delineation of the microscale processes of permeation in heterogeneous rock salt and may help in future to categorically evaluate the permeation behavior based on the microstructure.

Acknowledgements

The completion of this work involved a close partnership between MaP, IfG, Nobian and Geostructures. Unfortunately, Prof. Dr. Janos L. Urai passed away on May 28, 2023, while the ongoing experimental work discussed in this contribution was still in progress. A significant portion of the experimental design and interpretation relies on conversations we had with Janos, and the authors want to express their deepest gratitude for his substantial contribution to this research.

References

Bakker, R. R., Fazio, M., Benson, P. M., Hess, K. U., & Dingwell, D. B. (2016). The propagation and seismicity of dyke injection, new experimental evidence. *Geophysical Research Letters*, *43*(5), 1876-1883.

Barabasch, J., Schmatz, J., Klaver, J., Schwedt, A., & Urai, J. L., (2023). Large grain-size-dependent rheology contrasts of halite at low differential stress: evidence from microstructural study of naturally deformed gneissic Zechstein 2 rock salt (Kristallbrockensalz) from the northern Netherlands. Solid Earth, 14,(3) pp.271–291.

Baumann, T.S., Bérest, P., Brouard, B., ter Braack, M., den Hartogh, M., Kaus, B., Klaver, J., Oonk, P., Popov, A., Schmatz, J. and Urai, J.L., (2022). CCC-integrated multiscale study of salt cavern abandonment in the Netherlands. The Mechanical Behavior of Salt X, pp.567-576.

Bérest, P., Bergues, J., & Brouard, B., (1999). Review of static and dynamic compressibility issues relating to deep underground salt caverns. International Journal of Rock Mechanics and Mining Sciences, Vol 36 issue 8, pp.1031-1049.

Brouard, B., Bérest, P., & Durup, J. G., (2001). In situ salt permeability testing. In SMRI Fall 2001 Meeting, pp.7-10.

Burlini, L., Vinciguerra, S., Di Toro, G., De Natale, G., Meredith, P., & Burg, J. P. (2007). Seismicity preceding volcanic eruptions: New experimental insights. *Geology*, *35*(2), 183-186.

Chen, H., Wei, L., Peng, H. H., Deyi, J., & Liu, R., (2022). Investigations in Structural Evolution Characteristics during Crack Self-Healing of Damaged Rock Salt. Preprint.

Desbois, G., Urai, J., L., Pérez-Willard, F., Radi, Z., Offern, S., Burkart, I., Kukla, P., A., & Wollenberg, U., (2013). Argon broad ion beam tomography in a cryogenic scanning electron microscope: a novel tool for the investigation of representative microstructures in sedimentary rocks containing pore fluid. Journal of Microscopy 249 (3) pp.215-235.

Drury, M.R., Urai, J.L., (1990). Deformation-related recrystallization processes. Tectonophysics 172 (3–4) pp. 235-253,

Fokker, P. A., (1995). The behaviour of salt and salt caverns. PhD Thesis TU Delft.
Heeb, J., Healy, D., Timms, N. E., and Gomez-Rivas, E., (2023). Rapid hydration and weakening of anhydrite under stress: implications for natural hydration in the Earth's crust and mantle. Solid Earth, 14, pp.985–1003.

Houben, M.E., ten Hove, A., Peach, C. J., & Spiers C.J., (2013). Crack healing in rocksalt via diffusion in adsorbed aqueous films: Microphysical modelling versus experiments. Physics and Chemistry of the Earth, Parts A/B/C, Vol 64 pp.95-104.

Keith, S., B., Spieth, V., & Rasmussen J., C., (2017). Zechstein-Kupferschiefer Mineralization Reconsidered as a product of Ultra-Deep Hydrothermal, Mud-Brine Volcanism. IntertechOpen, Contributions to Mineralization Chapter.2.

Lux, K., H., (2005). Zum langfristigen Tragverhalten von verschlossenen solegefüllten Salzkavernen – ein neuer Ansatz zu physikalischer Modellierung und numerischer Simulation: Theoretische und laborative Grundlagen. Erdöl, Erdgas, Kohle 121, pp.414–422.

Schenk O., Urai J.L., (2004). Microstructural evolution and grain boundary structure during static recrystallization in synthetic polycrystals of Sodium Chloride containing saturated brine. Contributions to Mineralogy and Petrology 146, pp.671–682.

Schoenherr, J., Urai, J.L., Kukla, P.A., Littke, R., Schleder, Z., Larroque, J.-M., Newall, M.J., Al-Abry, N., Al-Siyabi, H.A., Rawahi, Z., (2007). Limits to the sealing capacity of rock salt: A case study of the infra-Cambrian ara salt from the south Oman salt basin. AAPG Bulletin 91, pp.1541–1557.

Schulze, O., Popp, T., & Kern, H. (2001). Development of damage and permeability in deforming rock salt. Engineering geology, 61(2-3),pp.163-180.

Peach, C., J., (1991). Influence of deformation on the fluid transport properties of salt rocks, PhD Thesis Utrecht University.

Popp, T., Kern, H., Schulze, O., (2001). Evolution of dilatancy and permeability in rock salt during hydrostatic compaction and triaxial deformation. Journal of Geophysical Research, Solid Earth, pp 4061-4078.

Popp, T., Minkley, W., Wiedemann, M., & Salzer, K. (2015). Gas-pressure-induced integrity of salt formations. Geological Society, London, Special Publications, 415(1), pp.107-122.

Urai, J. L., Schmatz, J. & Klaver, J., (2019). Over-pressured salt solution mining caverns and leakage mechanisms. Phase 1 Micro-Scale Report.

Wolters, R., Düsterloh, U., (2009). Weiterentwicklung der EDV-Software INFIL zur Simulation des druckgetriebenen Infiltrationsprozesses von Fluiden in ein nicht permeables Barrieren-Gebirge (Salinar). Final Report No. 02C1355. Technical University Clausthal, Clausthal, Germany.